Sheffield Hallam University

Sol-gel synthesis pathway and electrochemical performance of ionogels: A deeper look into the importance of alkoxysilane precursor

JANANI, R <http://orcid.org/0000-0002-3633-0488>, FARMILO, N <http://orcid.org/0000-0001-5311-590X>, ROBERTS, A <http://orcid.org/0000-0002-3920-9579> and SAMMON, Chris <http://orcid.org/0000-0003-1714-1726>

Citation:

Copyright and re-use policy

Sol-gel synthesis pathway and electrochemical performance of ionogels: A deeper look into the importance of alkoxysilane precursor

Ronak Janani[a], Nicolas Farmilo[a], Alexander Roberts[b] and Chris Sammon[a]*

[a] Materials & Engineering Research Institute, Sheffield Hallam University, Sheffield, S1 1WB, UK

[b] Institute for Future Transport and Cities, Coventry University, Coventry, CV1 5FB, UK

ABSTRACT

There is a great interest in the application of ionogels as electrolyte for energy storage devices due to their enhanced safety compared to conventional electrolytes. This work aims to shed light on an often-overlooked aspect of ionogel synthesis which is the impact of the precursors on the sol-gel reaction kinetics and the electrochemical properties of the resultant ionogels. Using time-resolved Raman spectroscopy the non-hydrolytic sol-gel synthesis of ionogels from four different alkoxysilane precursors were monitored. Their electrochemical performance as electrolyte for electric double-layer capacitors were characterised using cyclic voltammetry and electrochemical impedance spectroscopy. Our findings suggest that presence of ionic liquid does not impact the sol-gel process kinetics of all four formulations in the same manner. In addition, ionogel formulations with the longest gelation time demonstrated poor electrochemical properties caused by the further ingress of silica into the activated carbon electrodes. This was confirmed with EDX analysis.

Key words: Ionogels, Alkoxysilane, Raman spectroscopy, Electrochemical impedance spectroscopy, double-layer supercapacitors

1. Introduction

Ionic liquids (IL) are salts with melting points below 100°C and are exclusively made of cations and anions; meaning this class of salts does not require a solvent to be dissociated[1]. Since the discovery of air and water stable ionic liquids in 1992[2], there has been an increasing focus on these materials in the field of energy storage. Ionic liquids are able to operate within a larger potential window compared to organic electrolytes while overcoming the major safety issue associated with the commercial electrolytes used in energy storage devices (i.e. flammability and high vapour pressure)[3–6]. However, application of liquid electrolytes carries the possibility of leakage which can cause damage to the surrounding circuitry as well as being a potential health hazard to the consumer. This issue was briefly addressed by Chiu and Moore in a 2003 publication[7].

Recently, ionogels have attracted attention as a unique and versatile type of electrolyte for batteries and supercapacitors[8,9]. Ionogels are ionic liquids confined in a quasi-solid structure. Depending on the type and chemical composition of the ionogel, its mechanical characteristic can vary from rigid and brittle to soft and compliant[10,11]. Being confined prevents any problem associated with ionic liquid leakage while preserving its high ionic conductivity[12]. In addition, ionogels eliminate the need for a separator in electrochemical cells[13].

Being one of the main fabrication routes for ionogels, sol-gel processing has provided researchers with diversity and simplicity. Various formulations have been suggested for the encapsulating quasi-solid skeleton of ionogels. In some cases, two or more alkoxysilanes are combined to tune and enhance the mechanical strength of the ionogel[12,14]. One must understand the possible effects that the alkoxide precursor can have on the properties of the resultant gel in order to gain the ability to design a functional task-specific formulation. This requires monitoring the sol-gel process with and without ionic liquids and characterising the performance

of the resultant ionogel. Raman spectroscopy is a powerful characterisation technique that has been used in the past to monitor the evolution of different sol-gel systems. For example, Mulder and Damen employed Raman spectroscopy to monitor the evolution of hydrolysis and condensation reactions of tetraethoxysilane (TEOS) in the presence of ethanol[15]. Lee and Jen investigated the influence of formamide (CH_3NO) concentration on the gelation kinetics of tetramethoxysilane (TMOS) via an acid-catalysed hydrolytic sol-gel route[16]. Marino et al. utilised Raman spectroscopy to monitor the reaction of TEOS in the presence of various acids during a series of hydrolytic sol-gel processes[17]. More recently, Szczurek et al. investigated the growth of organically functionalised alkoxysilane networks using a combination of Raman spectroscopy and rheology[18]. However, there is limited information in the literature regarding the influence of gradual changes in the alkoxysilane on the non-hydrolytic sol-gel synthesis pathway of ionogels. The non-hydrolytic sol-gel route is more commonly reported in the literature for the fabrication of ionogel electrolytes which could be ascribed to the minimised volume of water in the electrolyte system. Generally, in non-hydrolytic sol-gel processing, the acid acts as both the solvent and the catalyst. Sharp who devised the non-hydrolytic sol-gel route, summarised the reactions taking place between an alkoxysilane and formic acid (FA) as follows[19]:

Carboxylation	[Si]OR + HOCOH	$\rightleftharpoons$	[Si]OCOH + ROH	(1.1)
	[Si]OH + HOCOH	$\rightleftharpoons$	[Si]OCOH + H_2O	(1.2)
Esterification	HOCOH + ROH	$\rightleftharpoons$	ROCOH + H_2O	(2.1)
Hydrolysis	[Si]OR + H_2O	$\rightleftharpoons$	[Si]OH + ROH	(3.1)
	[Si]OCOH + H_2O	$\rightleftharpoons$	[Si]OH + HOCOH	(3.2)
	[Si]OH + [Si]OCOH	$\rightarrow$	[Si]O[Si] + HOCOH	(4.1)
	[Si]OH + [Si]OH	$\rightarrow$	[Si]O[Si] + H_2O	(4.2)
Condensation	[Si]OH + [Si]OR	$\rightarrow$	[Si]O[Si] + ROH	(4.3)
	[Si]OR + [Si]OCOH	$\rightarrow$	[Si]O[Si] + ROCOH	(4.4)
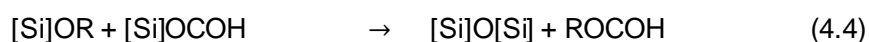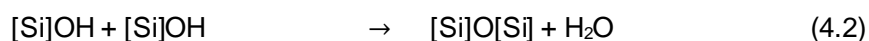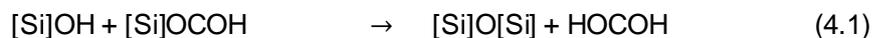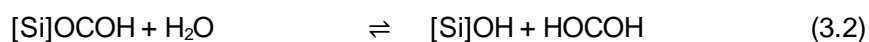
Where R, ROH and ROCOH groups represent alkyl, alcohol and alkyl formate groups, respectively. In some works reactions 4.2 and 4.3 are expressed as equilibria[20,21] since these reactions are reversible. Since various reactions can take place simultaneously in the investigated system, one must establish the formation and/or consumption kinetics of various compounds in the system in order to provide an understanding of the sol-gel process kinetics.

In an interesting investigation, Martinelli studied the non-hydrolytic sol-gel process pathway of a TMOS-based formulation in the presence and absence of ionic liquid[22]. Examples of such works are limited in the literature as most of the studies are focused on the physiochemical properties of the ionogels[12,23–25] after preparation and/or the effect of precursor-to-IL ratio on the electrochemical performance of ionogels[10,11,26]. This knowledge

gap has left one key question: Can the alkoxide precursor influence the properties and the electrochemical performance of ionogels? To shed light on this question, this work systematically investigates a series of alkoxysilanes to determine the influence of different precursors (in terms of the number of alkoxy groups and the chain length of the functional groups) on the sol-gel process kinetics with and without ionic liquid and the electrochemical performance of the resultant ionogels.

2. Experimental

2.1 Materials

Four different silicon alkoxides, namely tetramethylorthosilicate (TMOS, Sigma Aldrich, ≥98%) tetraethylorthosilicate (TEOS, Sigma Aldrich, ≥99%), methyltrimethoxysilane (MTMS, Sigma Aldrich, ≥98%) and methyltriethoxysilane (MTES, Sigma Aldrich, ≥99%) were utilised for xerogel and ionogel synthesis. Xerogels are solid structures prepared by drying wet gels via slow evaporation. The xerogels were synthesised using a simple non-hydrolytic sol-gel route and by mixing the alkoxide precursor with FA (Aldrich, ≥96%) in a 2:7 precursor-to-acid molar ratio at ambient conditions.

For ionogels, the synthesis was initiated by mixing 1-ethyl-3-methylimidazolium trifluoromethanesulfonate IL ([Emim][TfO], Sigma Aldrich, ≥98%) with the alkoxysilane precursor at a 1:1 molar ratio for 10 min under ambient conditions. This was followed by addition of FA (at 2:7 precursor-to-acid molar ratio) to the mixture. The final mixing time was varied between 3 (for Raman spectroscopy) to 10 minutes depending on the subsequent characterisation methods. All the chemicals were used as received.

2.2 Raman spectroscopy measurements

In order to monitor the chemical processes taking place in each sol-gel formulation, Raman spectra of each of the mixtures were collected at regular intervals. The first spectrum was collected after 3 minutes of mixing the alkoxysilane precursor (and IL in the case of ionogels) with FA. To do so, a 500 μL of the mixture was transferred into a stainless steel container using a micropipette. The subsequent spectra were collected at 10 minutes intervals for 2 hours. In the case of ionogels, additional spectra were collected after 6 and 12 hours. The focus of the laser beam was manually adjusted prior to each measurement. The early-stage sol-gel reaction pathway was monitored based on the evolution of peak height at selected wavenumbers.

In this work, Raman spectra were collected using an inVia Raman spectrometer (Renishaw, UK) using 785 nm diode laser excitation (10% laser power) and x5 objective (spot size ≈8 μm). Utilising the WiRE software (version 3.4), the exposure time and number of accumulations were set to 10 seconds and 1, respectively. Prior to the collection of data set, the device was calibrated using a silicon wafer (provided by Renishaw) in order to ensure accuracy of the spectral data.

2.3 EDLC Fabrication

After the 20 minutes mixing time described in section 2.1, 86, 100, 86 and 96 μL of TMOS-, TEOS-, MTMS- and MTES-ionogel, respectively was transferred onto activated carbon electrode discs (AC, WMG innovation centre, UK) with a mass loading of 1.8 mg cm^{-1}. The transferred volume of each ionogel corresponds to 36 μL of [Emim][TfO] on each electrode. The coated electrodes were then aged under ambient conditions until the

sol-gel transition point of the ionogel was reached i.e. 12 hours for TMOS- and TEOS-ionogels and 4 days for the MTMS- and MTES-ionogels. Two coated electrodes were crimped and tested immediately.

2.4 Electrochemical characterisation

A combination of cyclic voltammetry (CV) and electrochemical impedance spectroscopy (EIS) were utilised for the electrochemical performance analysis. The cyclic voltammetry (CV) analysis was conducted in a potential window of 2.5 V and at a scanning rate of 50 mV s^{-1}. The EIS measurements for EDLCs were conducted before and after 1000 CV cycles. For this, a 10 mV rms potential was applied oscillating around 0 V bias voltage over a frequency range of 100 kHz to 10 mHz. For ionic conductivity measurements ionogels were sandwiched between stainless steel current collectors. The CV and EIS measurements of the EDLC cells were obtained using a PARSTAT 4000A potentiostat (Princeton Applied Research, USA).

3. Results and discussions

3.1 Xerogels

As a primary step, Raman spectra for each of the reactants were collected and are displayed in Figure 1. Table 1 summarises the characteristic peaks of each of the chemicals and their corresponding assignments based on spectra displayed in Figure 1 and data available in the literature.

Having common functional groups between TMOS and MTMS, and between TEOS and MTES lead to Raman bands located at similar positions. As can be seen, the silicon alkoxide molecules have a strong Raman peak in the 627-653 cm^{-1} region which corresponds to the stretching vibration of the $Si-OC_xH_{2x+1}$ bond where an oxygen atom is bonded to an alkyl group. The stronger Raman intensity of this peak in TMOS and MTMS relative to that of TEOS and MTES are ascribed to the higher polarizability of $Si-O$ bonds in the methyl-based precursors [27].

Generally, the frequency of vibration depends on the masses of the atoms involved in the covalent bond and the strength of the bond. For instance, due to the substitution of a methyl group (in replacement of a methoxy group), the electron cloud around the silicon atom is altered. The $-CH_3$ groups have less electronegativity compared to that of $-OCH_3$ groups[28]. This results in a decrease on the partial charge on Si atom in MTMS compared to that in TMOS molecules which in turn reduces the $Si-OCH_3$ bond strength in MTMS and results in the small red shift of peaks in MTMS spectrum compared to that of TMOS and similarly to that of MTES compared to TEOS. Furthermore, the $C-H$ stretch regions of both TEOS and MTES are much more complex compared to that of the methyl-based precursors (TMOS and MTMS) as there are more different types of $C-H$ bonds available in their molecule. Additional $C-H$ stretching vibration bands are detected in Figure 1c and 1d at 2916 and 2914 cm^{-1}, respectively which is associated with the non-hydrolysable methyl group in MTMS[29] and MTES. The weak bands appearing at 854 and 739 cm^{-1} in the MTMS spectrum correspond to the rocking vibrations of CH_3 group in $Si-CH_3$[29].
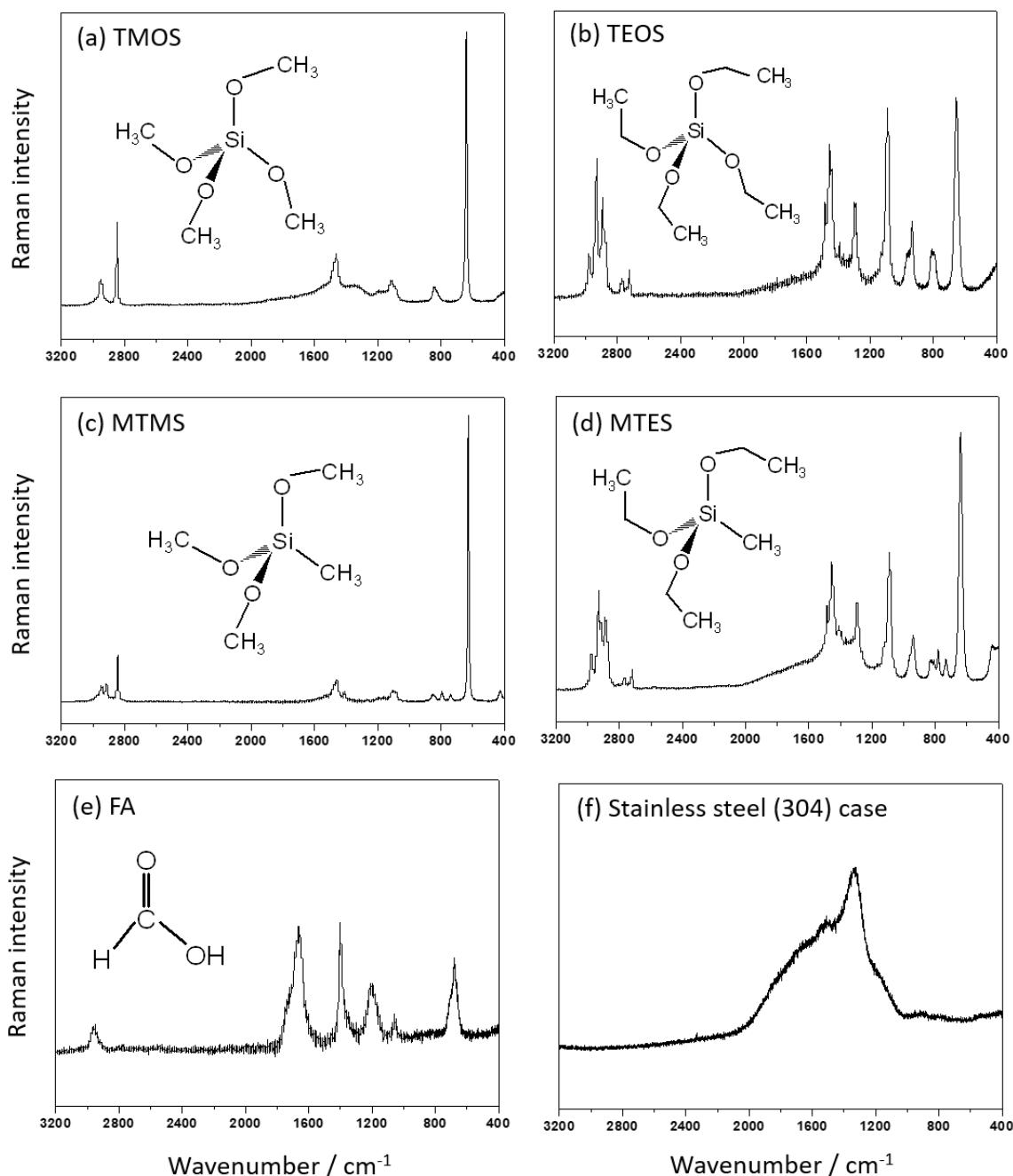
Figure 1 Raman spectra of (a) TMOS, (b) TEOS, (c) MTMS, (d) MTES, (e) FA and (f) 304 stainless steel container between 3200 and 400 cm^{-1} wavenumbers. The insets display the molecular structure of the precursors.

The Raman bands associated with FA (shown here in Figure 1e) have been reported in the past[16,30,31]. Similar to the Raman spectra of the alkoxides discussed earlier, the weak band at 2958 cm^{-1} in FA Raman spectrum is assigned to the C–H stretching vibration. More detailed peak assignments are provided in Table 1 based on similar works referenced in the Table. The two characteristic bands at 1330 and 1531 cm^{-1} in the stainless steel spectrum (shown in Figure 1f) originate from the D- and G-bands of the carbon content (0.07%) in the steel[32–34].

Table 1 Summary of selected vibrational modes and their corresponding assignments. The starred C−H bonds represent the case where C atom is directly connected to Si atom.

Compound	Wavenumber in this work (cm^{-1})	Wavenumber in other works (cm^{-1})	Assignment
TMOS	639	643[22,24], 642[30]	$\upsilon_s(Si-O)$
	843	845[16,30]	$\upsilon_{as}(Si-O)$
	2849	2845[30]	$\upsilon_s(C-H)$
	2951	2946[30]	$\upsilon_{as}(C-H)$
TEOS	653	654[15], 656[17]	$\upsilon_s(Si-O)$
	801	790[15]	$\upsilon_{as}(Si-O)$
	933	933[15]	$\upsilon_s(C-C)$
	962	960[15]	$\delta(C-H)$
	1089	1090[15]	$\upsilon(C-O)$
	2892	-	$\upsilon(C-H)$
	2935	-	$\upsilon(C-H)$
	2978	-	$\upsilon(C-H)$
MTMS	627	628[29]	$\upsilon_s(Si-O)$
	2845	2836[29]	$\upsilon_s(C-H)$
	2916	2916[29]	$\upsilon(C-H)^*$
	2948	2948[29]	$\upsilon_{as}(C-H)$
MTES	640	-	$\upsilon_s(Si-O)$
	2885	-	$\upsilon(C-H)$
	2914	-	$\upsilon(C-H)^*$
	2931	-	$\upsilon(C-H)$
	2976	-	$\upsilon(C-H)$
FA	676	677[30]	$\delta(O-C=O)$
	1203	1230[30]	$\upsilon(C-O)$
	1399	1382[30]	$\delta(H-C-O)$
	1667	1667[24,30]	$\upsilon(C=O)$
	2958	-	$\upsilon(C-H)$
304 stainless steel	1330	1320[34], 1350[32]	*D-band*
	1531	1594[34], 1580[32]	*G-band*

Figure 2 shows the reaction evolution of all four alkoxide precursors and FA within the first ≈2 hours of mixing the reactants. The arrows in this figure demonstrate the direction of time. As can be seen, the band intensity of the symmetric stretching vibration of Si−OC$_n$H$_{2n+1}$ (located between 627 and 653 cm^{-1}) that corresponds to the consumption of the silicon alkoxide, drops quickly. Depending on the precursor, each molecule contains between 3 to 4 −OC$_n$H$_{2n+1}$ branches and the reaction of one or more of these groups, results in a reduction of

the corresponding Raman peak intensity. Peak variations in the 650-720 cm^{-1} region are mainly attributed to the vibrations of Si−OC$_n$H$_{2n+1}$ bonds in partially hydrolysed precursors (as summarised by Winter et al.[35] and addressed in[15].) formed as a result of hydrolysis reactions. Consumption of FA partially contributes to the variations of Raman intensity in this region (i.e., δ(O−C=O) at 676 cm^{-1} as shown in Table 1). Formation of Si−O−Si bonds (attributed to a weak band between 474 and 489 cm^{-1}) marks the start and progress of the condensation process[22,30]. The variation in the position of this band between the four mixtures is attributed to structural difference between the final 3-dimensional silica networks. Formation of Si−O−Si bridges in the intermediate species gives rise to the detection of stretching vibrations of Si−O in the 500-610 cm^{-1} region[15,36]. Other highlighted bands in Figure 2b,d,f and h are related to the unequivocal signatures of alkyl formate (υ(O−C$_n$H$_{2n+1}$)) and alcohol (υ(C−O))[22,30]. The kinetics of formation and consumption of these species are studied in this work. Depletion of various Raman peaks in the 1350-1450 cm^{-1} and 1600-1800 cm^{-1} regions are related to the consumption of formic acid as a result of carboxylation and esterification reactions listed precisely as reactions 1.1, 1.2 and 2.1[22,30,31]. It is clear that Si−CH$_3$ bonds remain in the MTMS and MTES systems after the 2 hours experimental duration, as they do not participate in the sol-gel process.
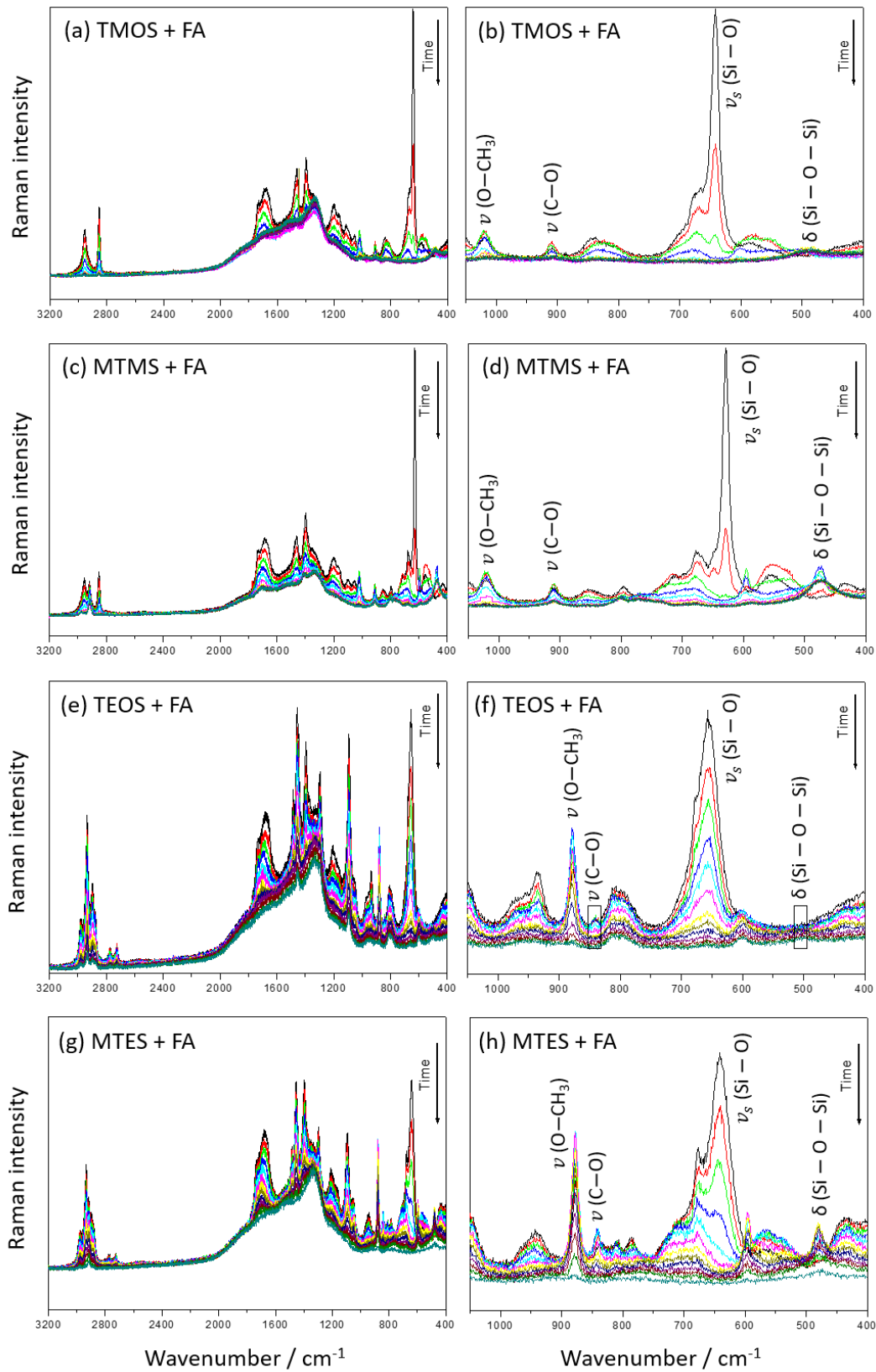
Figure 2 Raman spectra evolution with time of (a-b) TMOS, (c-d) MTMS, (e-f) TEOS and (g-h) MTES precursor and FA mixtures from t₀=3 minutes till t=2 hours from the mixing time.

The *in situ* monitoring of the sol-gel process in each formulation was performed by following the variations in the characteristic Raman intensity of key components in the mixture from $t_0 = 3$ minutes. These include: (a) the Si−O stretching mode of the silicon alkoxide located in the 627-653 cm^{-1} region, (b) characteristic peaks of ethyl and methyl formates (υ(C−O)) located in 840-841 and 909-910 cm^{-1} regions, respectively and (c) ethanol and methanol υ(O−C$_x$H$_{2x+1}$)) located at 877 and in 1018-1020 cm^{-1} region, respectively.

The reaction kinetic information was extracted from raw data by plotting the Raman intensity of the selected peaks as a function of time. A meaningful interpretation of data requires appropriate normalisation procedures (with respect to a 'reference peak') to account for differences in the surface properties and quality of focus during collection, loss of optical transmittance and evaporation of volatiles during the gelation process. For this purpose, the C−H stretching vibrations of the non-hydrolysable alkyl groups in MTMS and MTES (located at 2916 and 2914 cm^{-1}, respectively) were utilised for the initial stage of normalisation of the Raman data for their mixtures. However, data normalisation for TMOS and TEOS precursors are slightly more complicated as all of the covalent bonds available in their mixture go through transformation. This issue has been resolved in different ways in the past. Mulder and Damen studied a low-rate hydrolysis reaction of TEOS in ethanol and water and postulated that the rocking mode of the CH$_3$ group at 960 cm^{-1} does not undergo significant changes over time[15]. Other studies have been conducted in the presence of a non-reactive chemical (e.g. toluene[17] or ionic liquid[22]) to enable normalisation. In this work, the strong band at 1330 cm^{-1} attributed to the carbon content in the stainless steel containers was utilised for normalisation. This was done through precise peak fitting using Omnic software (version 9.6.238) to evaluate the correct peak intensity at 1330 cm^{-1}. The validity of this approach was examined and confirmed prior to further analysis. As the second and last step of normalisation, the maximum ($Raman\ intensity$) / ($Reference\ Peak\ intensity$) value in every dataset was identified and every data point in the same series was divided by this value. This resulted in all series having a maximum value of 1. To demonstrate repeatability, every measurement was performed in duplicate, and both were plotted as round 1 and 2 in the same graph.

Figure 3 represents the rate of precursor consumption (a-d), formation and consumption of methyl and ethyl formates (e-h) as well as methanol and ethanol (i-l) within a two-hour window from mixing each precursor with FA. These experimental results were shown to be repeatable. Based on Figure 3a-d, after ≈20 minutes of the sol-gel synthesis, Si−OR stretching vibration disappears in methyl-base precursor and acid mixtures while it takes between 40-100 minutes for this band to no longer be discernible from Raman spectra of the ethyl-based mixtures. As mentioned before, this band is attributed to the symmetric stretching vibration of Si−OR and its intensity is reduced when one or more of the these bonds are broken[15]. Thus, its disappearance cannot be regarded as the absence of Si−OR bonds in the sol mixture. In order to quantify the difference in the precursor consumption rate, zero order kinetics was assumed and therefore, a linear fit was plotted for each round of the υ_s(Si−O) time evolution measurements (for the linear region), the results of which are recorded in Table 2.
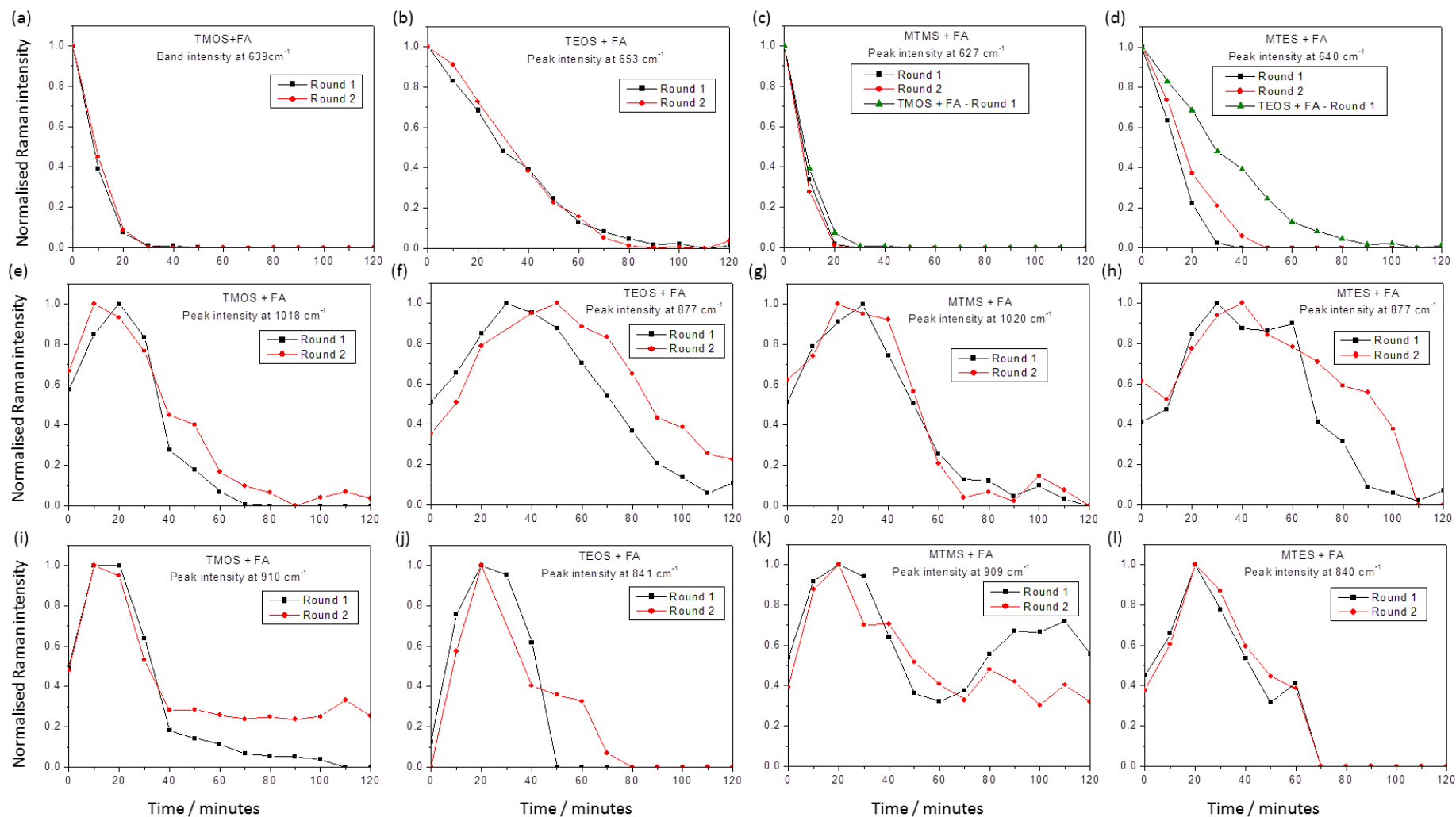
Figure 3 Time evolution of $\upsilon_s(Si-O)$ band in each of the mixtures (a-d) and the $\upsilon(C-O)$ bands associated with methanol and ethanol (e-h), and the alkyl formate groups (i-l).

10

Table 2 Linear fitting (Y= A + BX) information using Origin (version 6.0) software for time evolution of Si−OCₓH₂ₓ₊₁ band for each mixture.

Sample		B / minute^{-1}	R^2
TMOS+ FA	Round 1	(-49.04 $\pm$ 9.44)E-3	0.96
	Round 2	(-47.12 $\pm$ 6.26)E-3	0.98
TEOS+ FA	Round 1	(-12.33 $\pm$ 0.88)E-3	0.97
	Round 2	(-13.35 $\pm$ 0.87)E-3	0.98
MTMS+ FA	Round 1	(-49.12 $\pm$ 9.88)E-3	0.96
	Round 2	(-49.44 $\pm$ 13.18)E-3	0.93
MTES+ FA	Round 1	(-33.45 $\pm$ 3.27)E-3	0.98
	Round 2	(-24.08 $\pm$ 2.45)E-3	0.97

As can be seen from Table 2, $Si-OCH_3$ is consumed at a higher rate than $Si-OC_2H_5$. At the starting point of reaction monitoring (t_0=3 minutes) these bands can undergo chemical reactions 1.1 and 3.1[19]. Simultaneous to the carboxylation (reaction (1.1)), hydrolysis reaction (reaction (3.1)) can take place due to the presence of small volume of water ($\approx$4%) in commercial FA. At the start of the sol-gel process, reaction (3.1) is unlikely to take place as the alkoxysilane precursors are immiscible in water and require alcohol as a co-solvent[37]. This is due to the hydrophobic nature of the alkyl groups[38]. During the course of the reaction and as more water-soluble groups are formed, hydrolysis through reaction (3.1) becomes more likely. Since the hydrophobicity increases with the size of the alkyl chain, ethyl-based precursors require a larger volume of alcohol to solubil-ise in water. Therefore, consumption of ethyl-based precursors is expected to accelerate once enough ethanol is produced in the reaction environment and TEOS/MTES can participate in reaction (3.1) as well as reaction (1.1). Subsequently, the precursor participates in condensation reactions ((4.3) and (4.4)) and can be consumed in a wider range of routes. Thus, reaction (1.1) can be considered as the main route of precursor consumption in the early stages of the sol-gel process. During the non-hydrolytic sol-gel route, the oxygen atom in the alkoxy group undergoes protonic attack. This is the rate-determining step of the non-hydrolytic sol-gel process and is related to the electronegativity of the oxygen atom. In an interesting work done by Kanamori et al. [28] the partial charge of various alkoxysilanes was calculated using the 'partial charge model'. This model, proposed by Livage and Henry[39], suggests that the partial charge of an element can be calculated by considering the electronegativity of all of the elements present in the molecule (in neutral state). According to Kanamori et al. [28], the partial charge on oxygen atom in TMOS (-0.44) is slightly lower than that of TEOS (-0.46). The same is true for the case of MTMS (-0.46) and MTES (-0.47). This observation suggests that TMOS should have the slowest rate for reactions 1.1 and 3.1 while MTES should have the fastest rate. This does not agree with the observation made from Figure 3a-d and Table 2. This can be explained by considering the other influential factor in the protonic attack, steric hindrance. This phenomenon explains that due to the arrangement of atoms in a molecule, a longer alkyl chain hinders the protonic attack to the oxygen atom in the alkoxy chain. For this reason, the rate of TMOS and MTMS consumption are faster than those for TEOS and MTES by factors $\approx$4 and $\approx$1.7, respectively.

Based on Table 2, the average rate of precursor consumption in MTMS mixture ($B_{Average}$= -49.28E-3) is only slightly higher than that of TMOS mixture ($B_{Average}$ = -48.08E-3). This difference is much more noticeable for the MTES and TEOS mixtures. The substitution of an ethoxy group with an ethyl group is not expected to induce a reduction in the steric hindrance around the oxygen atoms in the remaining ethoxy groups. However, the partial charge on the oxygen atoms in MTES is slightly higher than that in TEOS. This is due to weaker electron withdrawing power of ethyl groups compared to ethoxy groups[28,40]. The higher electron density at oxygen atoms in MTES molecules makes this precursor more susceptible to protonic attack. Another factor influencing this considerable difference in the reaction kinetics among tetraalkoxysilanes and alkyltrialkoxysilanes is the stoichiometry of the carboxylation reaction. For every 1 mole of tetraalkoxysilane, 4 moles of FA is required for reaction (1.1) to take place while the precursor: FA molar ratio for alkyltrialkoxysilanes is 1:3 (as shown below).

$$R'_nSi(OR)_{4-n} + (4-n)HOCOH \rightleftharpoons R'_nSi(OCOH)_{4-n} + (4-n)ROH$$
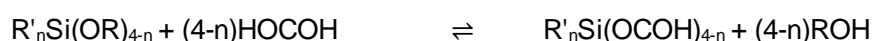
Because of the precursor: FA molar ratio used in this work (1:3.5), there is a stoichiometric imbalance for the case of TMOS and TEOS, while excess FA is present when MTMS and MTES are used. This mismatch contributes to the rate of the carboxylation process, which facilitates the alkoxide consumption. These results confirm that the early-stage sol-gel processes have progressed further in the case of methyl-based precursors compared to ethyl-based ones and follows the following order: MTMS≈TMOS>MTES>TEOS.

The rate of formation and consumption of methanol (for TMOS and MTMS) and ethanol (in TEOS and MTES-based mixtures) are displayed in Figure 3e-h. As can be seen, alcohol production reaches its peak after 20-50 minutes of the reaction monitoring period. The slower production of ethanol compared to methanol can be explained by the reduced rate of the carboxylation step (reaction (1.1)). This means that methanol is produced at a higher rate in methyl-based mixtures compared to ethanol in ethyl-based mixtures as a result of reactions (1.1) and (3.1).

Generally, alcohol can either be consumed through esterification (reaction 2.1) or leave the structure via evaporation. Methanol and ethanol have vapour pressures of 55.5 and 29.4 kPa at 50°C[41], respectively and thus, methanol is more volatile and more likely to leave the sol-gel mixture via evaporation compared to ethanol. On the other hand, as more methanol is formed in the system, the reaction equilibria in reactions 1.1, 2.1 and 3.1 is disturbed. Consequently, while the esterification reaction 2.1 yields more methyl formate to counterbalance the excess methanol, reactions (1.1) and (3.1) introduce more acid and alkoxide into the system. Due to the complex nature of the reactions, it is hard to confidently describe what takes place in the system at each point of time. However, based on Figure 3e-h, one can confidently state that methanol leaves the sol-gel system and/or is consumed at a higher rate compared to ethanol.

Figure 3i-l represents the consumption of the alkyl formate characteristic peak over time in each mixture. Generally, the methyl/ethyl formate is produced via reactions 2.1 and 4.4 which means alcohol and/or [Si]OCOH are required for the production of ROCOH groups. As the sol-gel process proceeds over time, more alcohol is introduced into the system disturbing the equilibrium of esterification reaction (2.1). Based on Le Chatelier's principle, the system will then adjust itself to counteract the excess ROH groups present in the system by producing more yield (water and ethyl/methyl formate) and establishing a new equilibrium. The results

shown in Figure 3i-l demonstrate a peak maximum in the formation of both methyl formate and ethyl formate after 20 minutes post mixing FA with the alkoxysilane.

A summary of the reactions involved in the consumption of [Si]OR and the formation of alcohol and alkyl formate is provided in Figure 4 (based on the reactions listed by Sharp[19]). Based on the Raman data shown thus far, one can presume that at the beginning of the non-hydrolytic sol-gel process, the alkoxysilane is mainly consumed via reaction 1.1 resulting in production of ROH groups. This then enables dissolution of the remaining alkoxysilanes (in water) and allows their consumption via reaction 3.1 (as well as 1.1) which introduces more ROH into the system. The peak alcohol production after 20-50 minutes of the reaction (see Figure 3e-h) may be caused by this dual production. Simultaneously, presence of alcohol enables the formation of alkyl formate groups via esterification (2.1) which peaks after 20 minutes (see Figure 3i-l). However, the complexity of the non-hydrolytic sol-gel process tempers any firm conclusion about the order of the reactions involved.
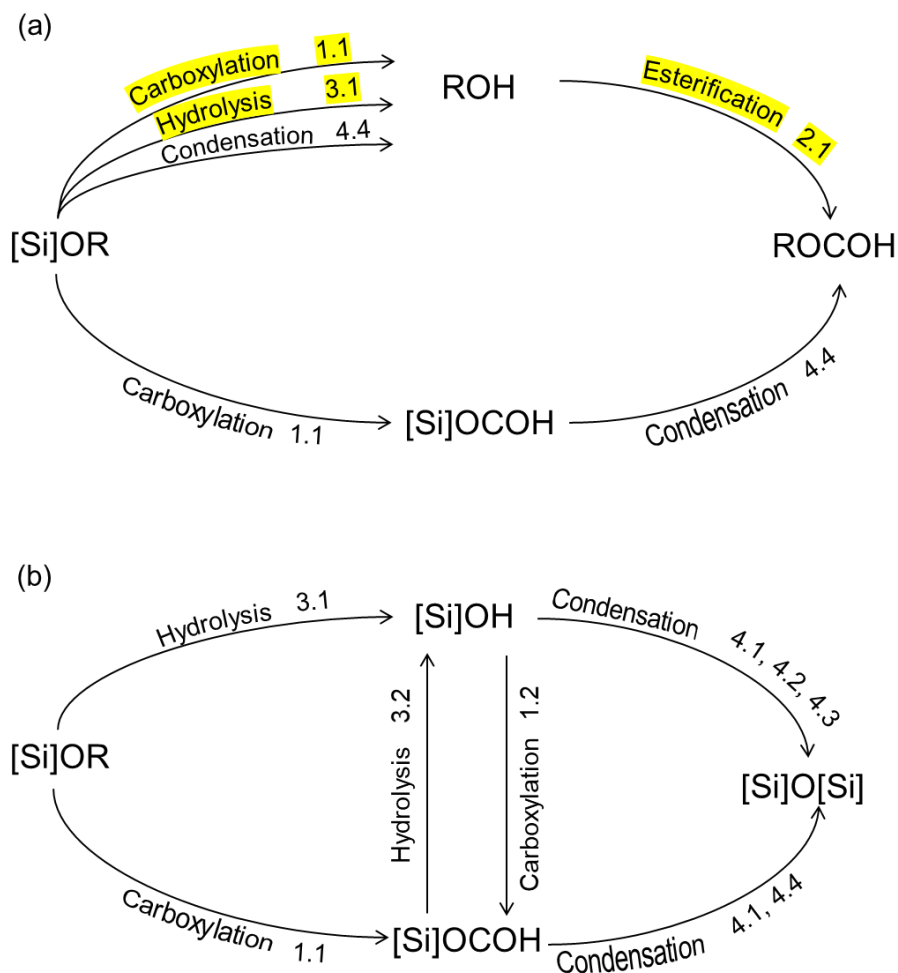

Figure 4 Summary of the reactions taking place in a non-hydrolytic sol-gel route adapted from the reactions listed by Sharp [19] (numbers represent the reaction number as listed in the introduction). The illustration shows the reactions involved in the (a) formation of methanol/ethanol (ROH) and methyl/ethyl formate (ROCOH) and (b) formation of [Si]O[Si]. The highlighted reactions are presumed to be rate limiting in this sol-gel process.

3.2 Ionogels

The molecular structure of [Emim][TfO] is shown in Figure 5a. This ionic liquid has a conductivity of 8.6 mS cm^{-1} (at room temperature) and a potential window of 4.3 V (manufacturer specification)[42]. At room temperature an average viscosity of 44 mPa s has been reported for this ionic liquid[43]. A pH of 6.6$\pm$0.1 has been reported for pristine [Emim][TfO] ionic liquid[44]. Trifluoromethanesulfonate anion has a single conformer which was favourable for this study to reduce the complexity of *in situ* investigation using Raman spectroscopy. Figure 5b and c display the Raman spectrum of this IL in the 300-3200 cm^{-1} region. Raman spectroscopy investigations of 1-Ethyl-3-methylimidazolium trifluoromethanesulfonate have been conducted in the past such as[45,46]. Table 3 provides a summary of the band assignments for this IL based on the current work and the data available in the literature.

From the lowest wavenumber, the vibrational bands at 313 and 348 cm^{-1} correspond to symmetric stretching vibrations of the C−S bond and the rocking mode of SO$_3$ of the anion[45]. Bands at 573, 756 and 597 cm^{-1} are associated with the antisymmetric and symmetric deformation vibrations of CF$_3$ and the oscillating vibrations of SO in the [TfO] anion, respectively[45,46]. The strong band at 1033 cm^{-1} is assigned to the symmetric stretching of S−O while its corresponding antisymmetric vibrational band is located at 1257 cm^{-1}[45,46]. The bands at 1169 and 1227 cm^{-1} correspond to the antisymmetric and symmetric stretching vibrations of C−F bonds in the anion, respectively[45]. The bands in the 1300-1600 cm^{-1} region are attributed to various vibrations within the imidazolium cation[46] which are listed in Table 3. The 2700-3050 cm^{-1} and 3050-3200 cm^{-1} regions are associated with the C−H stretching modes of alkyl chains (methyl and ethyl groups) and the C−H bonds within the ring (C(2)H, C(4)H, C(5)H) of the imidazolium cation[45,46].
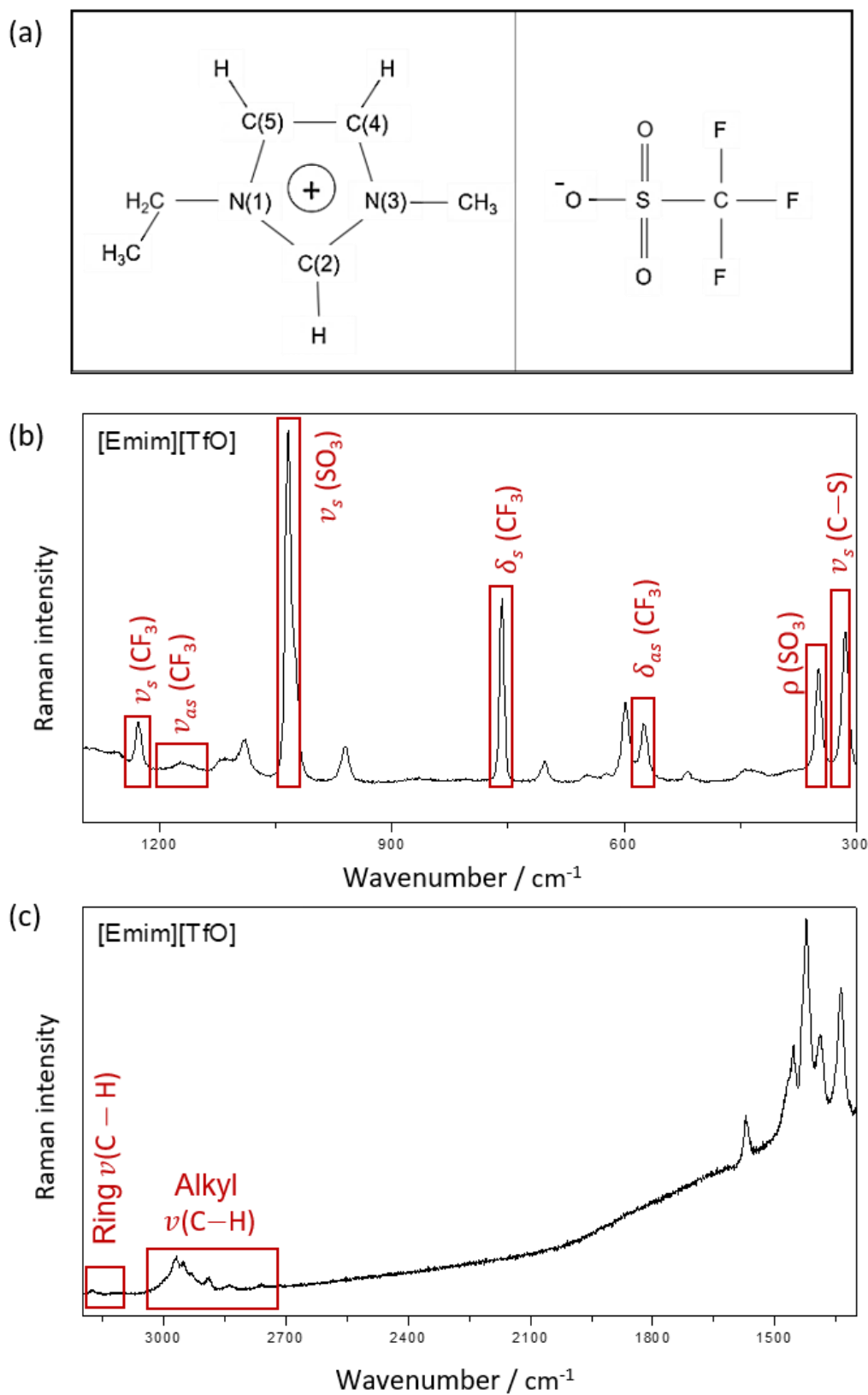
Figure 5 (a) Molecular structure of 1-ethyl-3-methylimidazolium cation (left) and trifluoromethanesulfonate anion (right) and Raman spectrum of [Emim][TfO] ionic liquid in the (b) 300-1300 cm^{-1}, (c) 1300-3200 cm^{-1} regions.

Table 3 Summary of selected vibrational modes of [Emim][TfO] and their corresponding assignments based on the results of the current investigation and the cited works.

Wavenumber in this work / cm^{-1}	Wavenumber in other works / cm^{-1}	Assignment
313	315 [45]	$\upsilon_s(CS)$
348	350 [45]	$\rho(SO_3)$
573	573 [45]	$\delta_{as}(CF_3)$
597	600 [46]	$\delta(SO)$
756	757 [45]	$\delta_s(CF_3)$
960	960 [46]	$\omega(NC(2)H)$
1033	1034 [45], 1033 [46]	$\upsilon_s(SO_3)$
1169	1173 [45]	$\upsilon_{as}(CF_3)$
1227	1230 [45]	$\upsilon_s(CF_3)$
1257	1260 [45]	$\upsilon_{as}(SO_3)$
1338	1337 [46]	$\rho(NCH),\ \tau(HC(7)H)$
1423	1424 [46]	$\upsilon(C(5)N),\ \delta(HC(6)H)$
1570	1570 [46]	$\upsilon(C(2)N),\ \upsilon(C=C),\ \rho(C(2,4)H)$
2768	2770 [46]	$\upsilon_s(CH_3)$
2889 & 2839	2890 & 2837 [46]	$\upsilon_s(C_2H_5)$
2931	2930 [46]	$\upsilon_{as}(CH_3)$
2971 & 2952	2971 & 2951 [46]	$\upsilon_{as}(C_2H_5)$
3118	3117 [45], 3116 [46]	$\upsilon_s(C(2)H)$
3177	3157 [45], 3171 [46]	$\upsilon_s(C(4,5)H)$

Figure 6 shows the evolving Raman spectra during the sol-gel process for all four formulations within the first ≈12 hours of mixing the reactants. The arrows demonstrate the direction of time. Similar to xerogels, an iono-gel was considered fully gelled (i.e. reached sol-gel transition point) when no flowing behaviour was observed upon agitation (using a spatula). Under ambient conditions, TMOS- and TEOS-based ionogels reached sol-gel transition point after 12 hours of synthesis while it took 4 days for full gelation to be achieved for MTMS- and MTES-based ionogels. Therefore, the reactions taking place inside all four mixtures were monitored for the first 12 hours of the synthesis. Based on the spectrum of 'as-received' [Emim][TfO] ionic liquid and that of the four ionogels, one can conclude that ionic liquid does not participate in the sol-gel process. However, Raman signals from ionic liquid dominate and interfere with the alkoxysilane and silica-related bands to some extent.

As the reaction proceeds the intensity of the strong bands between 642 and 628 cm^{-1} (symmetric stretching vibration of Si−OCH$_3$), which corresponds to the consumption of TMOS and MTMS, respectively are reduced quickly (Figure 6a-d). The peak variations in the 650-690 cm^{-1} region are mainly attributed to the vibrations of Si−OCH$_3$ bonds in partially hydrolysed precursor[35] and consumption of the FA ($\delta(O-C=O)$ at 676 cm^{-1})[30]. The vibrations in the 780-880 cm^{-1} region correspond to a combination of antisymmetric stretching vibrations

of Si$-$OCH$_3$ in and the Si$-$O vibrations of the intermediate species[15,22,36]. The stretching vibrations of C$-$O in methyl formate (located at 909 cm^{-1}) and O$-$CH$_3$ in methanol (located at 1020 cm^{-1}) are undetectable in the TMOS and MTMS-based ionogels' spectra. Depletion of various Raman peaks in the 1350-1450 cm^{-1} and 1600-1800 cm^{-1} regions are partially related to the consumption of FA as a result of carboxylation and esterification reactions[22,30,31]. In addition, the bending vibrations of C$-$H bonds present in methyl formate contribute to the Raman peaks in the 1440-1470 cm^{-1} region[22].

The Si$-$OC$_2$H$_5$ stretching vibrations (located at 662 and 640 cm^{-1} for TEOS and MTES mixtures, respectively) deplete at a lower rate compared to those of methyl-based precursors (Figure 6e-h). Furthermore, the bands located at 801 and 933 cm^{-1} which correspond to antisymmetric stretching of Si$-$O and symmetric stretching vibration of C$-$C in the alkoxide molecule, respectively [15] gradually disappear from the Raman spectra as the precursor is consumed. Due to low signal/noise ratio the unequivocal signature of ethyl formate (υ(C$-$O)) located at 841 cm^{-1} cannot be detected[17,47]. The υ(O$-$CH$_3$) vibrations assigned to ethanol at 877 cm^{-1} deplete within the first 2 hours of the experiment and cannot be detected after 6 hours suggesting that the majority of alcohol within the structure has either been consumed and/or evaporated. Variations of peaks in the 1000-1800 cm^{-1} are partly attributed to the consumption of FA via carboxylation and esterification reactions and the formation of ethyl formate.

The key difference between the spectra of corresponding tetraalkoxysilane and methyltrialkoxysilane-based mixtures is the presence of an additional C$-$H stretching vibration band at 2915 and 2914 cm^{-1} (according to their position after 2 hours) that originates from the non-hydrolysable methyl group available in MTMS- and MTES-based ionogels, respectively.

In order to compare the early-stage sol-gel process kinetics between the xerogels and the ionogels, the depletion rate of the υ_s(Si$-$O) band was evaluated (as shown in Figure 7). Since ionic liquid does not participate in the sol-gel process, the strong peak at 756 cm^{-1} associated with δ_s(CF$_3$) was used as the 'reference peak' for the normalisation process of the Raman data. In order to quantify the difference in the reaction rate, 0 order kinetics was assumed and therefore, a linear fit was plotted for each round of measurement, the results of which are recorded in Table 4.
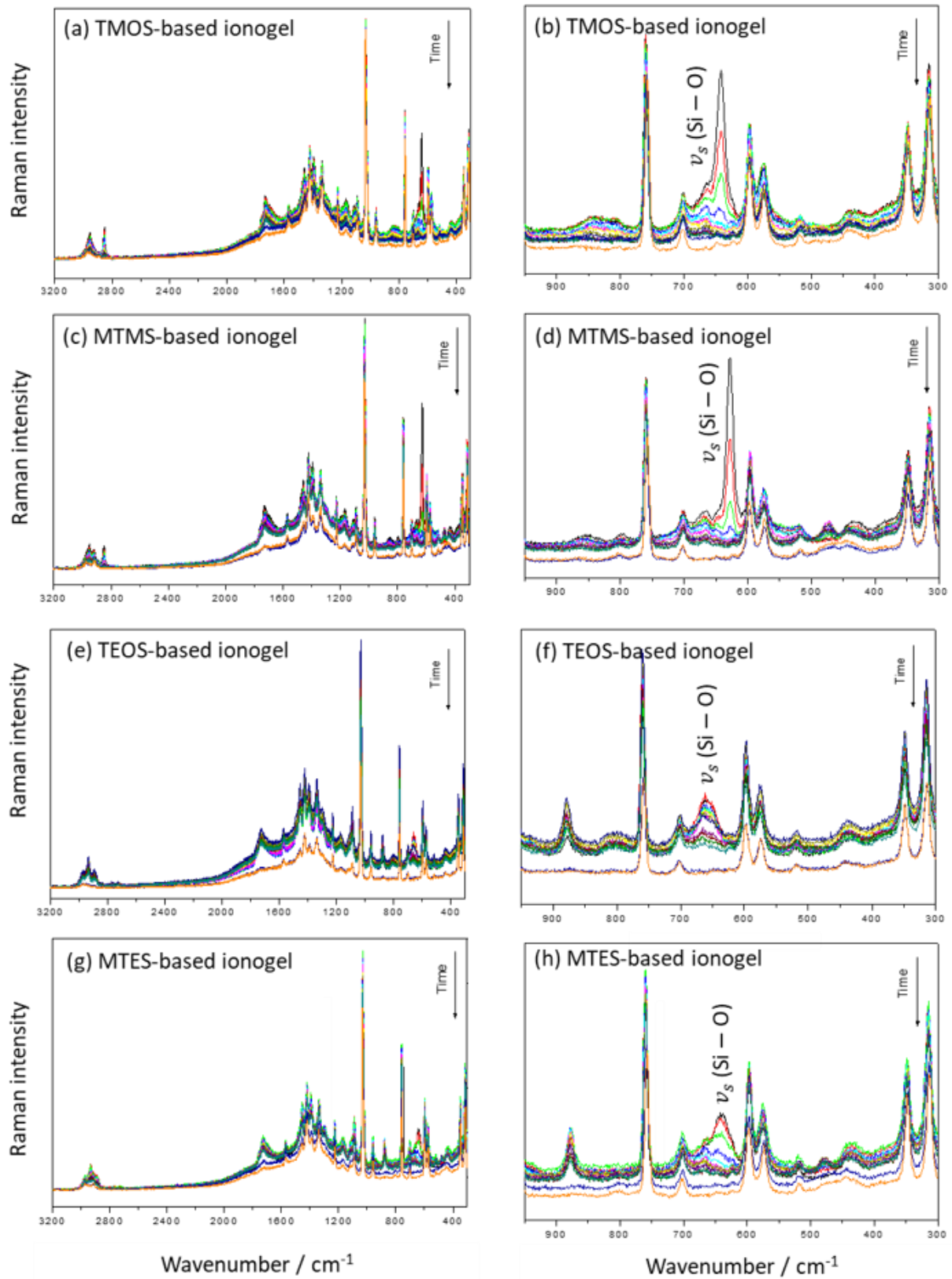
Figure 6 Raman spectra evolution with time of (a-b) TMOS-, (c-d) MTMS-, (e-f) TEOS- and (g-h) MTES-based ionogels from t_0=3 minutes up to t=12 hours from the mixing time.
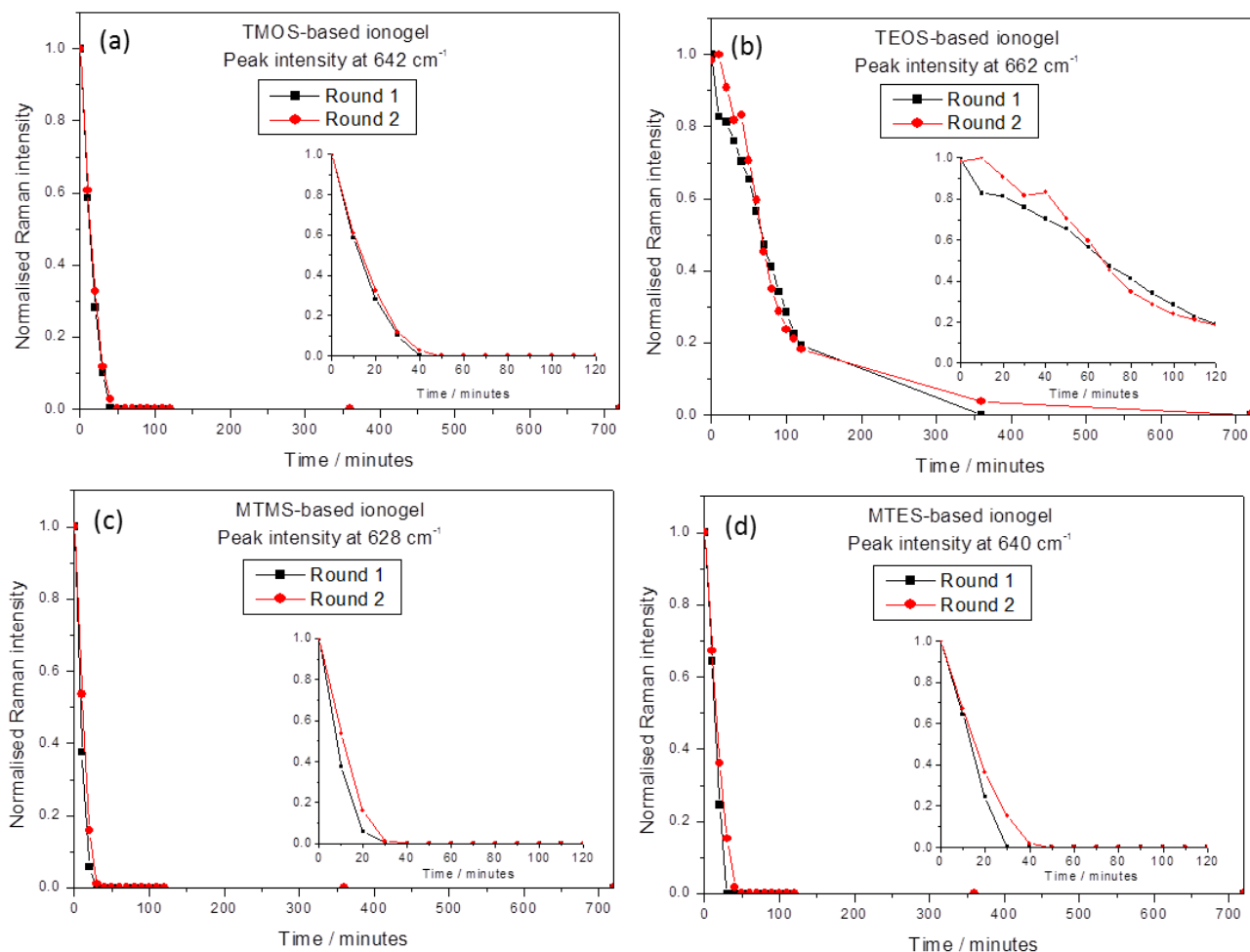
Figure 7 Time evolution of Si−O symmetric stretching mode in TMOS-, TEOS-, MTMS- and MTES-based ionogel mixtures. The expanded graphs of the intensity variations within the first two hours are provided in the insets.

Table 4 Linear fitting (Y= A + BX) information using Origin (version 6.0) software for time evolution of Si−OC_xH_{2x+1} band or each mixture.

Sample		B / minute^{-1}	R^2
TMOS ionogel	Round 1	(-30.0±3.7)E-3	0.97
	Round 2	(-29.3±3.0)E-3	0.98
TEOS ionogel	Round 1	(-6.6±0.2)E-3	0.99
	Round 2	(-7.8±0.4)E-3	0.97
MTMS ionogel	Round 1	(-47.1±8.9)E-3	0.97
	Round 2	(-33.5±5.1)E-3	0.96
MTES ionogel	Round 1	(-34.0±2.2)E-3	0.99
	Round 2	(-24.8±2.4)E-3	0.97

Similar to the earlier conclusion, reaction 1.1 is the main route for the alkoxysilane consumption in the early stages of the non-hydrolytic sol-gel process. Based on the fitting results recorded in Tables 2 and 4, the rate at which the band associated with Si–OC$_x$H$_{2x+1}$ stretching mode becomes indiscernible, drops when [Emim][TfO] ionic liquid is introduced to the sol-gel system for all mixtures except that of MTES. The process kinetic rate in the TMOS, TEOS and MTMS systems drops by 20-40% while no apparent change occurs in the initial consumption rate of MTES in its ionogel mixture. Martinelli and Nordstierna reported an increase in the consumption rate of TMOS when a small volume of an IL was introduced to the system (IL/TMOS molar ratio was 0.2)[30]. As described previously, and as shown in the Raman spectra of all samples in this work, ionic liquid does not participate in the sol-gel process. However, depending on its concentration, IL can dilute the sol mixture, change the environmental pH and retard the rate of oxygen protonic attack. Indeed, ILs have been suggested as a non-volatile drying control additive for sol-gel process to help control the rate of hydrolysis and condensation processes and reduce the mechanical stress exerted on the gel network during the drying stage (see section 3.3)[48,49]. Thus, It is plausible that at low concentrations, IL destabilizes the colloidal dispersion and accelerates particle aggregation and thus, the alkoxide consumption as shown in[30].

The overall alkoxide consumption rate of all four formulations has the following rank order: MTMS>TMOS≈MTES>TEOS with an average of ≈30% drop in the consumption kinetics of TMOS, MTMS and TEOS precursors compared to their xerogel counterparts (Tables 2 and 4). As discussed in section 3.1, the stoichiometry of the reaction, steric hindrance of the alkoxy chains and the difference in partial charge on the oxygen atom among the alkoxides contribute to the overall rate kinetics. It is probable that a balance of all these phenomena together with the presence of the IL, resulted in no overall variation in the MTES consumption kinetics. This proves that presence of IL does not influence the sol-gel process kinetics of different alkoxysilanes in the same manner and thus, this process must be investigated for each precursor independently.

3.3 Empirical observation

The physical structure of the xerogels and ionogels aged under ambient conditions are shown in Figure 8. Extensive shrinkage resulted in fractures in the TMOS- and TEOS-based xerogels while MTMS- and MTES-based xerogels showed a smooth surface with no apparent sign of shrinkage (Figure 8a-d). During the sol-gel process and as the volatile by-products leave the silica network (e.g. ROH and ROCOH groups), capillary pressure is exerted on the porous network. This is overcome by compressive stress on the solid structure which results in the shrinkage of the gels[50,51]. In addition, a typical porous silica network contains pores of various sizes and thus, as evaporation of volatile by-products takes place, a high pressure-gradient is created inside the network, causing collapse of capillaries. The presence of Si-CH$_3$ groups in the MTMS- and MTES-based gels reduces the surface tension of the alcohol and water within the pores[50] and reduce the crosslinking density of the silica network preventing capillary collapse.

The degree of gel shrinkage and the subsequent matrix collapse was reduced when IL was introduced into the silica system as shown in Figure 8e and f. This is ascribed to the ability of IL in forming a non-volatile film on the silica pore walls protecting the pores from drying stresses during evaporation of by-products[48,49]. Similar to xerogels, presence of the alkyl groups resulted in smooth MTMS- and MTES-based ionogels (Figure 8g and h).

As stated previously xerogels and ionogels were considered fully gelled (i.e. reached sol-gel transition point) when no flowing behaviour was observed upon agitation. Under ambient conditions, all xerogels reached full gelation within 2 hours of synthesis. However, TMOS- and TEOS-based ionogels reached sol-gel transition point after 12 hours of synthesis and it took 4 days for full gelation to be achieved for MTMS- and MTES-based ionogels.
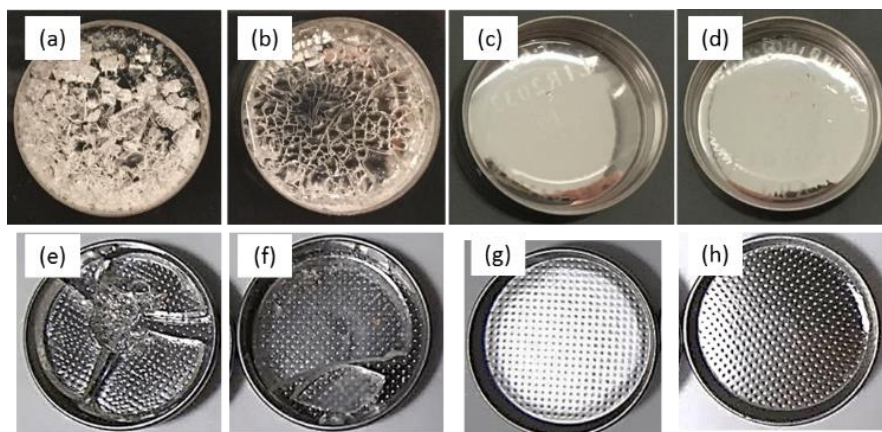

Figure 8 Optical images of (a-d) TMOS-, TEOS-, MTMS- and MTES-based xerogels, respectively and the corresponding ionogels (e-h). Images were taken after 2 hours and 4 days of aging (under ambient conditions) for xerogel and ionogel samples, respectively.

3.4 Application of the ionogels as EDLC electrolytes

Figure 9a shows the 1000th CV cycles of EDLCs with pristine IL and the ionogel electrolytes. The quasi-rectangular curves observed for cells with pristine IL and the TMOS and TEOS ionogels are indicative of fast charge propagation in the electrodes and good capacitive behaviour[52,53]. However, the CV curves for cells with MTES and MTMS ionogel electrolytes have more of an elliptical shape rather than quasi-rectangular. The distorted CV curves reflect resistive behaviour of the EDLCs and indicate that the cells behave more like a resistor rather than a supercapacitor[54]. This is also reflected in their areal capacitance values of 39.4 and 19.6 $mF\ cm^{-2}$, respectively compared to that of EDLCs with pristine IL (65.3 $mF\ cm^{-2}$), TMOS (54.5 $mF\ cm^{-2}$), and TEOS (60.4 $mF\ cm^{-2}$) ionogels. In some circumstances, the distortion of the CV curve can be attributed to 'electrolyte starvation', as described by Pell et al.[55] as the withdrawal of electrolyte charge carriers from the electrolyte bulk during the formation of double-layer. Although the underlying theory of this phenomenon supports the connection between the distortion of CV curves and an increase in the internal resistance of an electrochemical system, this is only limited to the cases in which the concentration of electrolyte is low. In this system as the same volume of ionic liquid was utilised in all of the EDLCs, electrolyte starvation can effectively be ignored.
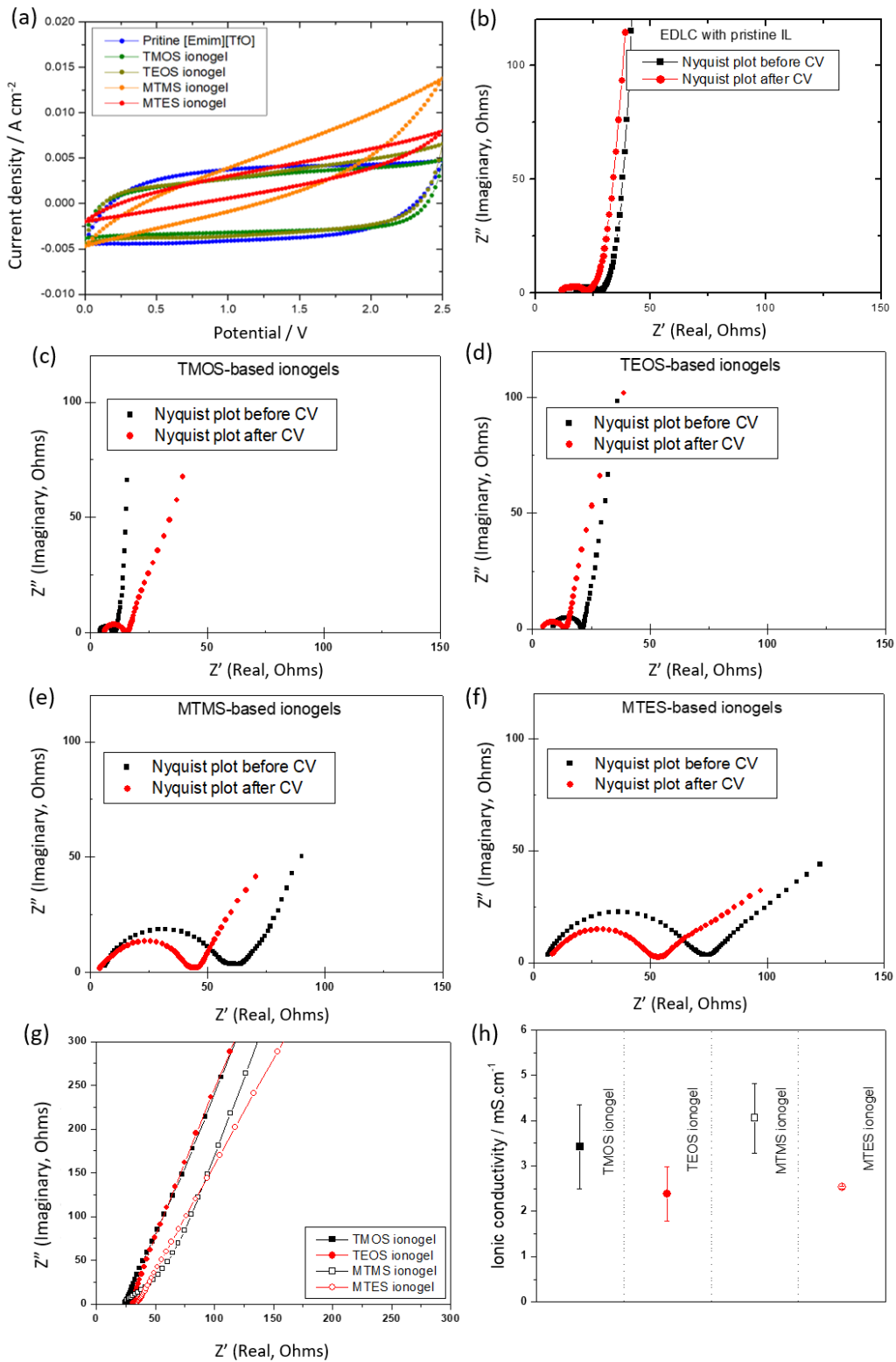
Figure 9 (a) The 1000th CV cycles of EDLCs with pristine [Emim][TfO], TMOS, TEOS, MTMS and MTES iono-gel electrolytes. (b-f) Nyquist plots of the EDLCs before and after 1000 CV cycles, (g) Nyquist plots of the four ionogels sandwiched between stainless steel current collectors, and (h) average ionic conductivities of each ionogel.

Figure 9b-f demonstrates the Nyquist plots of the EDLCs before and after the CV cycles. A Nyquist plot, generated from EIS measurements, demonstrates the real (x-axis) and imaginary components (y-axis) of impedance response of an electrochemical system at different charge-discharge frequencies and it is generally divided into 3 regions: low, mid-range and high frequency. In the high frequency region, the rate of charge-discharge cycle is too high for any mass transport to take place (100 kHz = $10^5 s^{-1}$ duration of one charge-discharge cycle). Therefore, the high frequency intercept resistance is a representation of both the bulk electrolyte resistance[56,57] and electrical contact resistance[58]. Since the electrochemical measurements were conducted at room temperature, ionic conductivity and thus, electrolyte resistance is expected to remain constant[53]. Consequently, the change in R_i in Figure 9b-f is attributed to a change in electrical contact resistance.

The charge transfer resistance (R_{ct}), given by the mid-range frequency semicircle, has been assigned to a number of ionic and electrical components inside an EDLC[55,59–62]. Studies have demonstrated that the dominating components influencing the R_{ct} are dependent on the system being investigated. Generally, systems containing ionic liquids are expected to have dominating ionic resistances influencing R_{ct} due to high viscosity and the relatively large size ionic liquid ions compared to regular salts. It is important to note that the nature of R_{ct} in EDLCs with porous electrodes[56,62] is different from that in psuedocapacitors which are mainly associated with the Faradaic processes taking place in the cell[60]. Based on our previous work with a similar ionogel system[63], R_{ct} is postulated to comprise of the ionic impedance components at: (i) the electrode-electrolyte interface and (ii) within the textural pores (i.e. inter-particle pores) of the AC electrodes.

As shown in Figure 9b-f, with the exception of the EDLCs with pristine IL and TMOS ionogel (where charge transfer remains unaltered) R_{ct} is reduced by 30-60% after the CV cycling. Previously, we have shown that the R_{ct} variations over time are assigned to the continuous increase in electrode wetted area by the electrolyte at the interface and the depth of the activated carbon[63]. The charging step of the CV cycles effectively increases the surface area between AC and ionic liquid, reducing the resistance (R) as per the following relationship[64,65]:

$R = \frac{L}{A \times \sigma}$ where L is the distance between the electrodes, A is the electrode area (permeated by the ionic liquid) and σ is the ionic conductivity. The L and σ parameters remain constant during the electrochemical measurements; therefore, changes in the resistance are associated with variation of the wetted area of the AC electrodes. Based on Figure 9c-f, R_{ct} is larger for EDLCs with MTMS and MTES ionogels compared to those of cells manufactured using TMOS and TEOS ionogels. This confirms that the lower capacitance values calculated for the two former systems are due to their larger internal resistance.

Furthermore, the low frequency region (linear region) in a Nyquist plot is assosiated with the intra-particle diffusion of electrolyte ions and double-layer formation[57,58]. The large inclining angle of the low frequency linear region (>45° with respect to x-axis) of the cells with pristine IL, TMOS and TEOS ionogels are an indication of good capacitive performance[58], which agrees well with their CV results shown in Figure 9a. For MTMS and MTES-based cells, the inclining angle of the low frequency region is ≤45° (Figure 9e-f). This can be attributed to diffusional limitation experienced by the cations and anions at low frequencies[66] and an increase in the distributed resistance in the AC electrodes[67] in cells containing MTMS and MTES ionogels.

To ensure that the observed difference in the electrochemical performance of the EDLCs is not an impact from possible IL-hosting matrix interactions[68], the complex impedance of the ionogels were measured while sandwiched between stainless steel current collectors (Figure 9g). When isolated from the porous AC electrode, the high frequency x-axis intercept in the Nyquist plot can be used to calculate ionic conductivity of the ionogels as per $\sigma = \frac{L}{A \times R}$ [53]. All four ionogels displayed an ionic conductivity of the same magnitude ranging between 2.5 to 4 mS.cm^{-1} (Figure 9h). Furthermore, the small variations in the ionic conductivities are independent of the R_{ct} changes observed in Figure 9c-f indicating that there is no correlation between the two phenomena.

Performing SEM with EDX analysis for elemental Si and Al (as a reference) across the cross section of TEOS and MTES ionogel-coated AC electrodes, it can be observed that silicon and thus, silica diffusion within the AC electrode is more pronounced compared to TEOS ionogel (Figure 10). This can be explained by the longer gelation time of MTES ionogel which provides more time for the mixture to permeate into the electrode. This is likely to cause pore blockage and an increase in the intrinsic resistance of the AC, as well as higher ionic resistance within AC electrodes. Because of the similarities observed between the gelation rate of the TMOS and TEOS ionogels and between MTMS and MTES ionogels, it can be considered that the electrodes coated with TEOS and MTES ionogels are representative of those of TMOS and MTMS ionogels, respectively.

Based on the CV curves of the MTMS- and MTES-based cells and the EDX results one can speculate that the diffusion of silica into the AC electrode not only blocks inter-particle pores but also influences the intra-particle pores which results in less pronounced capacitive behaviour and more resistive characteristic that is observed in both CV (and its elliptical shape) and EIS (large semicircle and low inclining angle of the low frequency region) results.
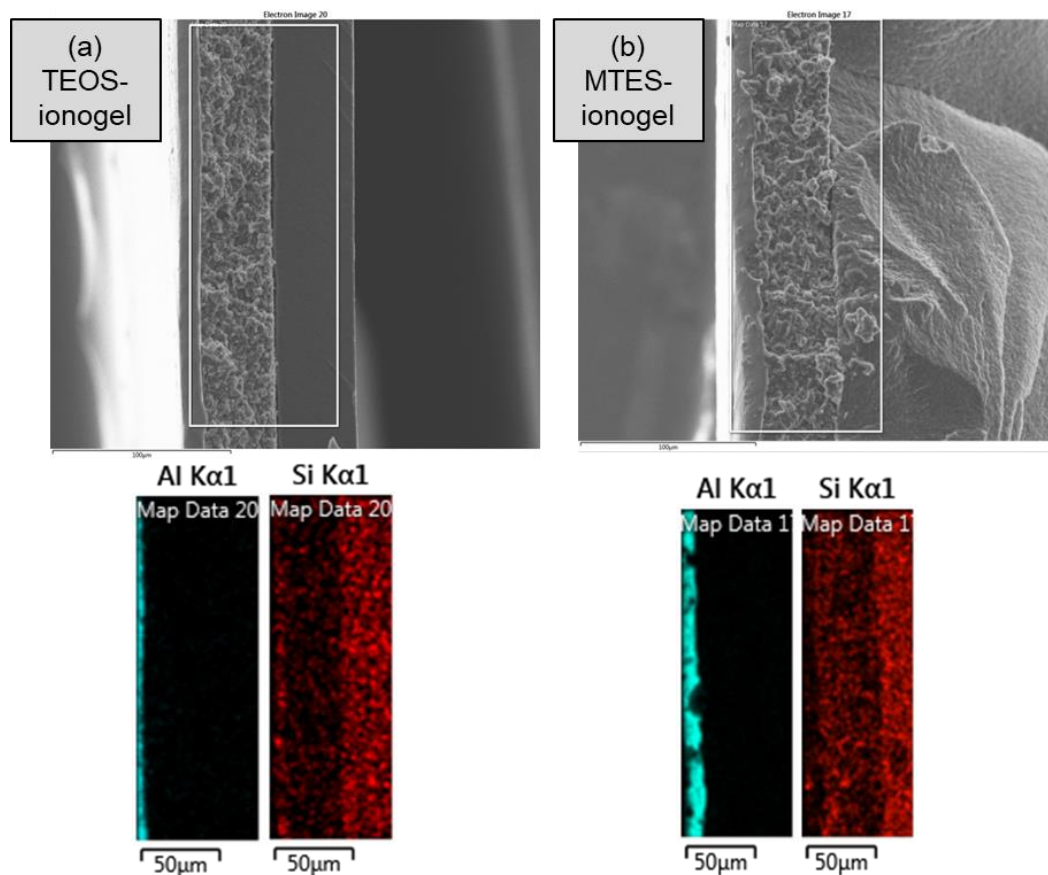
Figure 10 Distribution of aluminium (the current collector) and silicon (from the ionogel) at the AC electrode and the (a) TEOS ionogel and (b) MTES ionogel interface detected using EDX.

Evidently, longer gelation imposes the risk of silica ingress into the porous electrode which can result in a reduction of the electrode active surface area. Furthermore, a longer gelation time is not desirable from an industrial perspective and can have a negative impact on the production cost. For these reasons, TMOS- and TEOS-based ionogels seem to be most suitable candidates of those in this study for the electrochemical application. However, extensive shrinkage of these ionogels over time (Figure 8e and f) can result in the loss of electrode-ionogel contact and jeopardize the lifetime of the resultant EDLC. Mixing different alkoxysilanes together is often a way to improve the mechanical properties of the resultant ionogel[12,14]. However, attention must be paid to the compatibility of the precursors, as poor choice can result in heterogeneity in the gel (the more reactive precursor forms silica networks faster). Based on the reaction kinetics investigated in this work, TMOS and MTMS are the most compatible precursors in terms of the initial sol-gel process kinetics in the presence of IL. This study suggests that the choice of alkoxysilane as the precursor for ionogels for solid state electrolytes should not be taken lightly.

4. Conclusions

This work investigated the effects of systematic change in the alkoxysilane precursor on the early-stage sol-gel process, gelation rate and the electrochemical performance of the resultant ionogel. Raman spectroscopy conducted as a function of reaction time showed a 20-40% reduction in the consumption rate of the TMOS, TEOS and MTMS when IL was introduced into the sol. Stoichiometry of the reaction, steric hindrance of the

alkoxy chains and the difference in partial charge on the oxygen atom among the alkoxides contributed to the overall consumption rate of the precursors. The presence of IL is considered to retard the oxygen protonic attack and the condensation rate by diluting the sol. However, no difference in the consumption rate of MTES was detected when IL was present in the sol which indicated that IL did not influence every formulation in the same way. It was also shown that the gelation of MTMS and MTES ionogels take place ≈8 times slower than TMOS and TEOS ionogels. One important finding was that the slow gelation of MTMS and MTES ionogels caused considerable ingress of silica into the electrode reducing the effective surface area. This negatively impacted the capacitive behaviour of the corresponding EDLCs. While TMOS and TEOS-based ionogels showed enhanced electrochemical performance, their extensive shrinkage under ambient conditions raises concerns about the shelf-life or the long-term performance of their EDLCs. By incorporating non-hydrolysable groups into the gel network, the capillary tension, shrinkage, and brittleness of ionogels can be reduced. This can be achieved by mixing the tetraalkoxysilanes with alkyltrialkoxysilanes. These findings suggest that the alkoxysilane precursor(s) can impact the ionogel production rate as well as its electrochemical performance and thus, care must be taken in choosing the most suitable formulation.

Declaration of competing interest

The authors declare that they have no known competing financial interests or personal relationships that could have appeared to influence the work reported in this paper.

References

1. Singh MP, Singh RK, Chandra S. Ionic liquids confined in porous matrices: Physicochemical properties and applications. *Prog Mater Sci*. 2014;64:73-120. doi:10.1016/j.pmatsci.2014.03.001

2. Wilkes JS, Zaworotko MJ. Air and water stable 1-ethyl-3-methylimidazolium based ionic liquids. *J Chem Soc Chem Commun*. 1992;(13):965-967. doi:10.1039/C39920000965

3. Zhu Q, Song Y, Zhu X, Wang X. Ionic liquid-based electrolytes for capacitor applications. *J Electroanal Chem*. 2007;601(1-2):229-236. doi:10.1016/j.jelechem.2006.11.016

4. Eftekhari A. Supercapacitors utilising ionic liquids. *Energy Storage Mater*. 2017;9(September):47-69. doi:10.1016/j.ensm.2017.06.009

5. Buzzeo MC, Evans RG, Compton RG. Non-haloaluminate room-temperature ionic liquids in electrochemistry - A review. *ChemPhysChem*. Published online 2004. doi:10.1002/cphc.200301017

6. Galiński M, Lewandowski A, Stępniak I. Ionic liquids as electrolytes. *Electrochim Acta*. 2006;51(26):5567-5580. doi:10.1016/J.ELECTACTA.2006.03.016

7. Chiu Y-T, Moore SK. Leaking capacitors muck up motherboards. *IEEE Spectr*. 2003;40(2):16-17. doi:10.1109/MSPEC.2003.1176509

8. Chen N, Zhang H, Li L, Chen R, Guo S. Ionogel Electrolytes for High-Performance Lithium Batteries: A Review. *Adv Energy Mater.* 2018;8(12):1702675. doi:10.1002/aenm.201702675

9. Gupta SK, Gupta S, Gupta AK. Ionogels: Present Opportunities, and Challenges for Future in Energy Storage Applications. *Adv Sci Eng Med.* 2020;12(16):11-26. doi:https://doi.org/10.1166/asem.2020.2516

10. Horowitz AI, Panzer MJ. High-performance, mechanically compliant silica-based ionogels for electrical energy storage applications. *J Mater Chem.* 2012;22(32):16534-16539. doi:10.1039/C2JM33496H

11. Horowitz AI, Westerman K, Panzer MJ. Formulation influence on the sol-gel formation of silica-supported ionogels. *J Sol-Gel Sci Technol.* 2016;78(1):34-39. doi:10.1007/s10971-015-3918-7

12. Néouze MA, Le Bideau J, Gaveau P, Bellayer S, Vioux A. Ionogels, new materials arising from the confinement of ionic liquids within silica-derived networks. *Chem Mater.* 2006;18(17):3931-3936. doi:10.1021/cm060656c

13. Brachet M, Brousse T, Le Bideau J. All solid-state symmetrical activated carbon electrochemical double layer capacitors designed with ionogel electrolyte. *ECS Electrochem Lett.* 2014;3(11):A112-A115. doi:10.1149/2.0051411eel

14. Bengourna N, Despetis F, Bonnet L, et al. Textural, structural and electrical characterizations of EMIMAc silica ionogels and their corresponding aerogels. *Appl Phys Res.* 2014;6(4):16-25.

15. Mulder CAM, Damen AAJM. Raman analysis of the initial stages of the hydrolysis and polymerization of tetraethylorthosilicate. *J Non Cryst Solids.* 1987;93(1):169-178. doi:10.1016/S0022-3093(87)80036-4

16. Lee YT, Jen HH. A Raman study of the effect of formamide on the tetramethoxysilane sol–gel process. *J Non Cryst Solids.* 2004;342(1-3):39-45. doi:10.1016/J.JNONCRYSOL.2004.07.009

17. Marino I-G, Lottici PP, Bersani D, Raschellà R, Lorenzi A, Montenero A. Micro-Raman monitoring of solvent-free TEOS hydrolysis. *J Non Cryst Solids.* 2005;351(6-7):495-498. doi:10.1016/J.JNONCRYSOL.2004.11.023

18. Szczurek A, Paszkowski M, Lewandowski D, Gąsiorek J, Kaleta J, Krzak J. Organically functionalized sol-gel silica network growth. *Ceram Int.* 2020;46(9):13198-13204. doi:10.1016/j.ceramint.2020.02.094

19. Sharp KG. A two-component, non-aqueous route to silica gel. *Sol-Gel Sci Technol.* 1994;2:35-41.

20. Brinker CJ. Hydrolysis and condensation of silicates: Effects on structure. *J Non Cryst Solids.* 1988;100(1-3):31-50. doi:10.1016/0022-3093(88)90005-1

21. Bogush GH, Zukoski IV CF. Studies of the kinetics of the precipitation of uniform silica particles through the hydrolysis and condensation of silicon alkoxides. *J Colloid Interface Sci.* 1991;142(1):1-18. doi:10.1016/0021-9797(91)90029-8

22. Martinelli A. Effects of a protic ionic liquid on the reaction pathway during non-aqueous sol–gel synthesis of silica: A Raman spectroscopic investigation. *Int J Mol Sci*. 2014;15(4):6488-6503. doi:10.3390/ijms15046488

23. Gupta AK, Verma YL, Singh RK, Chandra S. Studies on an ionic liquid confined in silica nanopores: Change in Tg and evidence of organic-inorganic linkage at the pore wall surface. *J Phys Chem C*. 2014;118(3):1530-1539. doi:10.1021/jp408142a

24. Nayeri M, Aronson MT, Bernin D, Chmelka BF, Martinelli A. Surface effects on the structure and mobility of the ionic liquid C6C1ImTFSI in silica gels. *Soft Matter*. 2014;10(30):5618-5627. doi:10.1039/C4SM00642A

25. Sert Çok S, Koç F, Balkan F, Gizli N. Revealing the pore characteristics and physicochemical properties of silica ionogels based on different sol-gel drying strategies. *J Solid State Chem*. 2019;278(June). doi:10.1016/j.jssc.2019.07.038

26. Taubert A, Löbbicke R, Kirchner B, Leroux F. First examples of organosilica-based ionogels: Synthesis and electrochemical behavior. Schneider JJ, ed. *Beilstein J Nanotechnol*. 2017;8:736-751. doi:10.3762/bjnano.8.77

27. Larkin P. Chapter 2 – Basic Principles. In: *Infrared and Raman Spectroscopy*. ; 2011:7-25. doi:10.1016/B978-0-12-386984-5.10002-3

28. Kanamori K, Nakanishi K. Controlled pore formation in organotrialkoxysilane-derived hybrids: From aerogels to hierarchically porous monoliths. *Chem Soc Rev*. 2011;40(2):754-770. doi:10.1039/C0CS00068J

29. Baatti A, Erchiqui F, Bébin P, Godard F, Bussières D. A two-step sol-gel method to synthesize a ladder polymethylsilsesquioxane nanoparticles. *Adv Powder Technol*. 2017;28(3):1038-1046. doi:10.1016/j.apt.2017.01.009

30. Martinelli A, Nordstierna L. An investigation of the sol-gel process in ionic liquid-silica gels by time resolved Raman and 1H NMR spectroscopy. *Phys Chem Chem Phys*. 2012;14(38):13216-13223. doi:10.1039/C2CP41914A

31. Nayeri M, Nygård K, Karlsson M, et al. The role of the ionic liquid C6C1ImTFSI in the sol–gel synthesis of silica studied using in situ SAXS and Raman spectroscopy. *Phys Chem Chem Phys*. 2015;17(15):9841-9848. doi:10.1039/C5CP00709G

32. Feng H-P, Hsu C-H, Lu J-K, Shy Y-H. Effects of PVD sputtered coatings on the corrosion resistance of AISI 304 stainless steel. *Mater Sci Eng A*. 2003;347(1-2):123-129. doi:10.1016/S0921-5093(02)00578-6

33. Esteves M, Ramalho A, Ramos F. Fretting behavior of the AISI 304 stainless steel under different atmosphere environments. *Tribol Int*. 2015;88:56-65. doi:10.1016/J.TRIBOINT.2015.02.016

34. Janković A, Eraković S, Mitrić M, et al. Bioactive hydroxyapatite/graphene composite coating and its corrosion stability in simulated body fluid. *J Alloys Compd.* 2015;624:148-157. doi:10.1016/J.JALLCOM.2014.11.078

35. Winter R, Chan J, Frattini R, Jonas J. The effect of fluoride on the sol-gel process. *J Non Cryst Solids.* 1988;105:214-222.

36. Lippert JL, Melpolder SB, Kelts LM. Raman spectroscopic determination of the pH dependence of intermediates in sol-gel silicate formation. *J Non Cryst Solids.* 1988;104(1):139-147. doi:10.1016/0022-3093(88)90193-7

37. Gnado J, Dhamelincourt P, Pélégris C, Traisnel M, Le Maguer Mayot A. Raman spectra of oligomeric species obtained by tetraethoxysilane hydrolysis-polycondensation process. *J Non Cryst Solids.* 1996;208(3):247-258. doi:10.1016/S0022-3093(96)00526-1

38. Wheeler G. *Alkoxysilanes and the Consolidation of Stone.* Vol 46. C. Hudson; 2005. doi:10.1007/s13398-014-0173-7.2

39. Livage J, Henry M. *Ultrastructure Processing of Advanced Ceramics.* (Mackenzie JD, Ulrich DR, eds.). John Wiley and Sons; 1988. https://www.osti.gov/servlets/purl/7250006

40. Tan B, Rankin SE. Study of the effects of progressive changes in alkoxysilane structure on sol–gel reactivity. *J Phys Chem B.* 2006;110(45):22353-22364. doi:10.1021/jp060376k

41. Moilanen P, Uusi-Kyyny P, Pokki J-P, Pakkanen M, Aittamaa J. Vapor-liquid equilibrium for butane + methanol, + ethanol, + 2-propanol, + 2-butanol, and + 2-methyl-2-propanol (TBA) at 323 K. *J Chem Eng Data.* 2008;53(1):83-88. doi:10.1021/je7003947

42. Ionic liquids for electrochemical applications. Aldrich ChemFiles. Published 2005. Accessed June 20, 2018. https://www.sigmaaldrich.com/technical-documents/articles/chemfiles/ionic-liquids-electrochemical.html

43. Zhang S, Lu X, Zhou Q, Li X, Zhang X, Li S. Imidazolium. In: *Ionic Liquids, Physiochemical Properties.* Elsevier; 2009:23-197. doi:10.1016/B978-0-444-53427-9.00002-6

44. Ge X, Li J, Zhang C, Wang Z, Luo J. Superlubricity of 1-ethyl-3-methylimidazolium trifluoromethanesulfonate ionic liquid induced by tribochemical reactions. *Langmuir.* 2018;34(18):5245-5252. doi:10.1021/acs.langmuir.8b00867

45. Liu Z, El Abedin SZ, Endres F. Raman and FTIR spectroscopic studies of 1-ethyl-3-methylimidazolium trifluoromethylsulfonate, its mixtures with water and the solvation of Zinc ions. *ChemPhysChem.* 2015;16(5):970-977. doi:10.1002/cphc.201402831

46. Singh DK, Rathke B, Kiefer J, Materny A. Molecular structure and interactions in the ionic liquid 1-ethyl-3-methylimidazolium trifluoromethanesulfonate. *J Phys Chem A.* 2016;120(31):6274-6286.

doi:10.1021/acs.jpca.6b03849

47. Panitz J-C, Wokaun A. Characterization of the sol-gel process using Raman spectroscopy organically modified silica gels prepared via the formic acid-alkoxide route. *J Sol-Gel Sci Technol.* 1997;9(3):251-263. doi:10.1007/BF02437188

48. Klingshirn MA, Spear SK, Holbrey JD, Rogers RD. Ionic liquids as solvent and solvent additives for the synthesis of sol-gel materials. *J Mater Chem.* 2005;15(48):5174. doi:10.1039/b508927a

49. Vioux A, Viau L, Volland S, Le Bideau J. Use of ionic liquids in sol-gel; ionogels and applications. *Comptes Rendus Chim.* 2010;13(1):242-255. doi:https://doi.org/10.1016/j.crci.2009.07.002

50. Pisal AA, Rao AV. Comparative studies on the physical properties of TEOS, TMOS and Na2SiO3 based silica aerogels by ambient pressure drying method. *J Porous Mater.* 2016;23(6):1547-1556. doi:10.1007/s10934-016-0215-y

51. Brinker CJ, Scherer GW. *Sol-Gel Science: The Physics and Chemistry of Sol-Gel Processing.*; 1990. doi:10.1186/1471-2105-8-444

52. El-Kady MF, Kaner RB. Scalable fabrication of high-power graphene micro-supercapacitors for flexible and on-chip energy storage. *Nat Commun.* 2013;4:1475-1479. doi:10.1038/ncomms2446

53. Negre L, Daffos B, Turq V, Taberna PL, Simon P. Ionogel-based solid-state supercapacitor operating over a wide range of temperature. *Electrochim Acta.* 2016;206(Supplement C):490-495. doi:https://doi.org/10.1016/j.electacta.2016.02.013

54. Fontaine O, Touidjine A, Maréchal M, et al. A one-pot route to prepare class II hybrid ionogel electrolytes. *New J Chem.* 2014;38(5):2008-2015. doi:10.1039/C3NJ01272G

55. Pell WG, Conway BE, Marincic N. Analysis of non-uniform charge/discharge and rate effects in porous carbon capacitors containing sub-optimal electrolyte concentrations. *J Electroanal Chem.* 2000;491(1-2):9-21. doi:10.1016/S0022-0728(00)00207-2

56. Lei C, Markoulidis F, Ashitaka Z, Lekakou C. Reduction of porous carbon/Al contact resistance for an electric double-layer capacitor (EDLC). *Electrochim Acta.* 2013;92:183-187. doi:10.1016/J.ELECTACTA.2012.12.092

57. Yoo HD, Jang JH, Ryu JH, Park Y, Oh SM. Impedance analysis of porous carbon electrodes to predict rate capability of electric double-layer capacitors. *J Power Sources.* 2014;267:411-420. doi:10.1016/J.JPOWSOUR.2014.05.058

58. Basri NH, Deraman M, Suleman M, et al. Energy and power of supercapacitor using carbon electrode deposited with nanoparticles nickel oxide. *Int J Electrochem Sci.* 2016;11:95-110.

59. An KH, Kim WS, Park YS, et al. Electrochemical properties of high-power supercapacitors using single-walled carbon nanotube electrodes. *Adv Funtional Mater.* 2001;11(5):387-392.

doi:10.1002/1616-3028(200110)11:5<387::AID-ADFM387>3.0.CO;2-G

60. Gu T, Wei B. Fast and stable redox reactions of MnO2/CNT hybrid electrodes for dynamically stretchable pseudocapacitors. *Nanoscale*. 2015;7(27):11626-11632. doi:10.1039/c5nr02310f

61. Yang I, Kim SG, Kwon SH, Lee JH, Kim MS, Jung JC. Pore size-controlled carbon aerogels for EDLC electrodes in organic electrolytes. *Curr Appl Phys.* 2016;16(6):665-672. doi:10.1016/j.cap.2016.03.019

62. Yang I, Kim S-G, Kwon SH, Kim M-S, Jung JC. Relationships between pore size and charge transfer resistance of carbon aerogels for organic electric double-layer capacitor electrodes. *Electrochim Acta*. 2017;223:21-30. doi:10.1016/J.ELECTACTA.2016.11.177

63. Janani R, Mader K, Roberts AJ, Farmilo N, Sammon C. Fast-cure ionogel electrolytes with improved ion transport kinetics at room temperature. *J Power Sources*. 2018;406:141-150. doi:10.1016/j.jpowsour.2018.10.049

64. Wu MS, Liao TL, Wang YY, Wan CC. Assessment of the wettability of porous electrodes for lithium-ion batteries. *J Appl Electrochem*. 2004;34(8):797-805. doi:10.1023/B:JACH.0000035599.56679.15

65. Kühnel RS, Obeidi S, Lübke M, Lex-Balducci A, Balducci A. Evaluation of the wetting time of porous electrodes in electrolytic solutions containing ionic liquid. *J Appl Electrochem*. 2013;43(7):697-704. doi:10.1007/s10800-013-0558-x

66. Wang H, Xu Z, Kohandehghan A, et al. Interconnected carbon nanosheets derived from hemp for ultrafast supercapacitors with high energy. *ACS Nano*. 2013;7(6):5131-5141. doi:10.1021/nn400731g

67. Ruch PW, Cericola D, Foelske-Schmitz A, Kötz R, Wokaun A. Aging of electrochemical double layer capacitors with acetonitrile-based electrolyte at elevated voltages. *Electrochim Acta*. 2010;55(15):4412-4420. doi:10.1016/j.electacta.2010.02.064

68. Olivier-Bourbigou H, Magna L, Morvan D. Ionic liquids and catalysis: Recent progress from knowledge to applications. *Appl Catal A Gen*. 2010;373(1-2):1-56. doi:10.1016/J.APCATA.2009.10.008